

Direct Observations of Structural Phase Transitions in Planar Crystallized Ion Plasmas

T. B. Mitchell, J. J. Bollinger, X.-P. Huang and W. M. Itano

Time and Frequency Division, National Institute of Standards and Technology, Boulder, CO 80303

D. H. E. Dubin

Department of Physics, University of California at San Diego, La Jolla, CA 92093

R. H. Baughman

Allied Signal Inc., Research and Technology, Morristown, NJ 07962, USA

Laser-cooled $^9\text{Be}^+$ ions confined into two-dimensionally extended lattice planes were directly observed, and the images used to characterize their structural phases. Five different stable crystalline phases were observed, and the energetically favored structure could be sensitively tuned by changing the areal density of the confined ions. The experimental results are in good agreement with predictions from theory for the planar (infinite in two dimensions) one-component plasma. Qualitatively similar structural phase transitions occur, or are predicted to occur, in other experimentally realizable planar systems.

The one-component plasma (OCP) has been an important model of condensed matter in statistical physics for over 30 years, and is used to describe such diverse systems as dense astrophysical matter (1) and electrons on the surface of liquid helium (2). Laser-cooled, trapped ions (3) are an excellent experimental realization of the OCP. The phase structure of spatially homogeneous (infinite) (4) and cylindrical (5) (infinite in one dimension only) OCPs have been explored previously. Here, images of individual ions confined in two-dimensionally extended lattice planes are presented, and are used to characterize the structural phases with the observed structure agreeing well with the predictions of an analytic theory for the planar OCP.

The OCP model consists of a single charged species embedded in a uniform, neutralizing background charge. In Paul (6) or Penning (6,7) traps, which are used to confine charged particles, a (fictitious) neutralizing background is provided by the confining potentials. The thermodynamic properties of the infinite classical OCP are determined by its Coulomb coupling parameter

$$\Gamma \equiv \frac{1}{4\pi\epsilon_0} \frac{e^2}{a_{WS}k_B T}, \quad (1)$$

which is the ratio of the Coulomb potential energy of neighboring ions to the kinetic energy per ion. Here, ϵ_0 is the permittivity of the vacuum, e is the charge of

an ion, k_B is Boltzmann's constant, T is the temperature, and a_{ws} is the Wigner-Seitz radius, defined by $4\pi(a_{ws})^3/3 = 1/n_0$ where n_0 is the ion density. The onset of short-range order for the infinite OCP is predicted (8) at $\Gamma \approx 2$, and a phase transition to a body-centered cubic (bcc) lattice is predicted (8,9) at $\Gamma \approx 170$. With an OCP in a planar geometry (infinite in only two directions), boundary effects are predicted to cause the formation of a variety of additional structural phases, such as the hexagonal-close-packed (hcp) and face-centered-cubic (fcc) phases (10–12). Qualitatively similar structural phase transitions occur, or are predicted to occur, in other planar systems with varied interparticle interactions, such as plasma dust crystals (13), colloidal suspensions (14), semiconductor electron bilayer systems (15) and hard spheres (16).

The crystallization of small numbers (total number $N < 50$) of laser-cooled ions into Coulomb clusters (17) was first observed in Paul traps (18). With larger numbers of trapped ions, concentric shells (19) were directly observed in Penning (20) and Paul traps (5,21). Recently, Bragg diffraction has been used to detect bcc crystals, the predicted infinite volume ordering, in large and spherical ($N > 2 \times 10^5$, radius $r_0 > 60a_{ws}$) ion plasmas confined in a Penning trap (4).

We present measurements from direct images of the central ($r=0$) structure of pancake-shaped (lenticular) ion plasmas (aspect ratio $\alpha \equiv z_0/r_0 < 0.1$, where $2z_0$ is the plasma center's axial extent). The central region has a “disk-like” geometry with constant areal density σ (charge density per unit area projected onto the $z = 0$ plane), which facilitates comparison with planar theory. We observe five different stable crystalline phases, finding that the energetically favorable central structure can be tuned by changing the central areal density σ_0 of the plasma. Both continuous and discontinuous structural phase transitions are observed.

The $^9\text{Be}^+$ ions were confined in a cylindrical Penning trap (Fig. 1, inner trap diameter 40.6 mm) with a uniform magnetic field $B=4.465$ T in the \hat{z} -axis direction to confine the ions radially. The ions were confined axially by a potential difference of $V_0 = -1.50$ kV applied between the center and end electrodes of the trap.

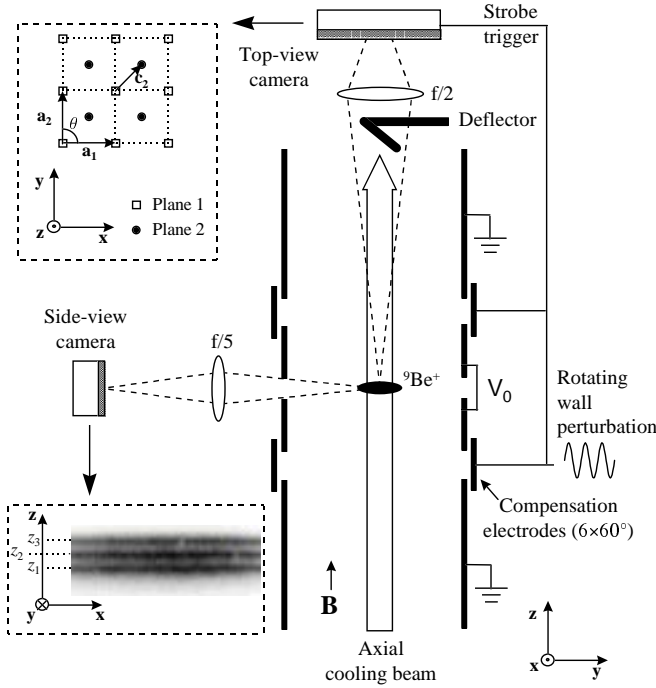


FIG. 1. Schematic side view of the cylindrical Penning trap with its side- and top-view imaging optics. The insets show the variables used to characterize the intra- and interlayer structure. The side-view inset also shows the central region of a lenticular ion plasma with three axial lattice planes.

Near the trap center this axial potential is quadratic and has a value of $1/2(m/e)\omega_z^2 z^2$, where the axial frequency $\omega_z/2\pi = 978$ kHz for ${}^9\text{Be}^+$. The radial electric fields of the trap as well as the ion space charge cause the ion plasma to undergo an $\mathbf{E} \times \mathbf{B}$ drift and thus rotate about the trap axis. In thermal equilibrium, this rotation is at a uniform frequency ω_r . The radial binding force of the trap is determined by the Lorentz force caused by the plasma's rotation through the magnetic field. Thus, low ω_r results in a weak radial binding and a lenticular plasma with a large radius. For 10^4 trapped ions with $\omega_r/2\pi = 68.5$ kHz (typical for this work), the ion plasma has a density of $2.1 \times 10^8 \text{ cm}^{-3}$ with $2r_0 \approx 1.3$ mm and an aspect ratio $\alpha \approx 0.05$. The rotation frequency was controlled by phase-locking the plasma rotation to an applied “rotating wall” electric field (22). At low ω_r , an increase in ω_r increases the plasma density and z_0 , thus providing a way to sensitively adjust the central areal density of the plasma.

The ions are cooled (3) by a laser beam propagating along the z axis and tuned 10–20 MHz lower in frequency than a hyperfine-Zeeman component of the $2s^2S_{1/2} \rightarrow 2p^2P_{3/2}$ resonance at 313 nm with a natural linewidth of 19 MHz. The laser power is approximately 50 μW and is focused at the ion plasma to a diameter of about 0.5 mm. The theoretical cooling limit is 0.5 mK,

while an experimental upper bound of $T < 10$ mK has been measured (23). For a density of $n_0 = 2 \times 10^8 \text{ cm}^{-3}$, these give a range of $160 < \Gamma < 3150$. A series of lenses form side- and top-view images of the ions, with viewing directions perpendicular and parallel to the magnetic field respectively, on either a gateable charge-coupled device (CCD) camera, or on an imaging photomultiplier tube. The resolution of the optical systems is $\approx 4 \mu\text{m}$, while typical interparticle spacings are $\approx 20 \mu\text{m}$.

The side-view image inset in Fig. 1, which shows the central region of a lenticular ion plasma with three axial lattice planes, is representative of the flatness and radial extent ($< 10\%$ of r_0) of this region. At large radius, curvature of the planes can cause the side-view images of axial plane positions to blur. This effect was prevented in the measurements reported here by using clouds with sufficient amounts (up to 50%) of non-fluorescing impurity ions. Because these heavier-mass ions are centrifugally separated to larger radii than the ${}^9\text{Be}^+$, the regions of the plasma where curvature begins to be significant can be filled with these ions, which are sympathetically cooled by the ${}^9\text{Be}^+$ (24).

With good alignment of the trap with the magnetic field ($< 10^{-3}$ radians), the ion plasma rotation is phase-locked with the “rotating wall” perturbation (22). Direct observation of the rotating ion structures was achieved for the first time by gating the top-view CCD camera synchronously with the “rotating wall” perturbation for gate times brief ($< 2\%$) relative to the plasma rotation period. Total exposure times of $\approx 3 \times 10^4$ rotation periods were used in typical images (Fig. 2). For our study of the ion lattice structure we limited our analysis to the central region, where strong localization and regular ordering of the ions is observed. At larger radius we observe an increased blurring due to the plasma rotation, occasional lattice distortions, and ultimately the transition to the regions filled by heavier-mass ions.

The observed structure of the central crystallized region depends on the central areal density σ_0 of the plasma. Within a layer, the lattice is characterized by the primitive vectors \mathbf{a}_1 and \mathbf{a}_2 (which are observed to be equal in magnitude, $|\mathbf{a}_1| = |\mathbf{a}_2| \equiv a$), or equivalently by a and the angle θ ($\leq 90^\circ$) between the primitive vectors. The interlayer structure is characterized by the axial positions z_n of the n lattice planes (measured by the side-view camera) and the interlayer displacement vector \mathbf{c}_n between layers 1 and n . Hence, the equilibrium (x, y) positions of ions in axial planes 1 and n are given by $\mathbf{R}_1(\mathbf{i}, \mathbf{j}) = \mathbf{i}\mathbf{a}_1 + \mathbf{j}\mathbf{a}_2$ and $\mathbf{R}_n(\mathbf{i}, \mathbf{j}) = \mathbf{i}\mathbf{a}_1 + \mathbf{j}\mathbf{a}_2 + \mathbf{c}_n$, where \mathbf{i}, \mathbf{j} are integers.

Three different types of intralayer ordering are observed: hexagonal ($\theta = 60^\circ$), square ($\theta = 90^\circ$) and rhombic ($90^\circ > \theta \geq 65^\circ$). The square and rhombic layers stack in a staggered fashion, with upper ions immediately above the centers of the parallelograms below, resulting in an interlayer displacement vector $\mathbf{c}_2 = (\mathbf{a}_1 + \mathbf{a}_2)/2$.

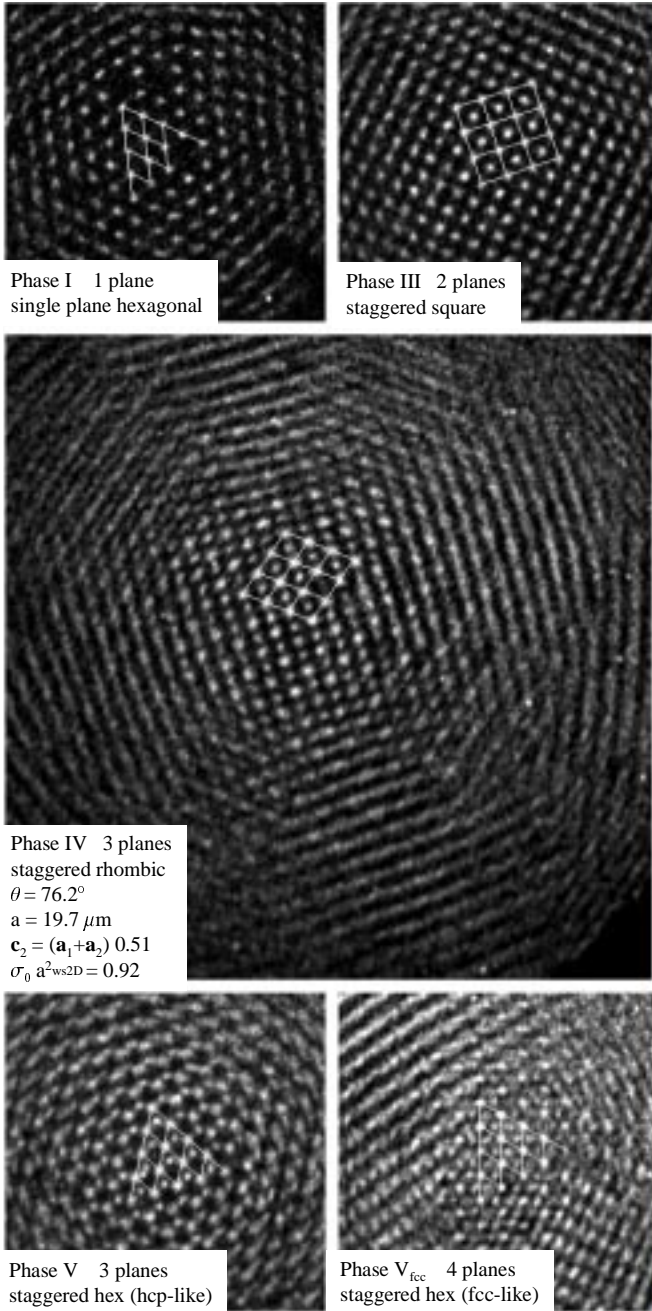


FIG. 2. Top-view (x, y) images of the five structural phases observed in the experiment, with lines showing a fit of the central ions to the indicated structure.

Hexagonal layers similarly stack with ions above the centers of the triangles below, but there are two distinct ways of doing this, $3\mathbf{c}_2 = \mathbf{a}_1 + \mathbf{a}_2$ and $3\mathbf{c}_2/2 = \mathbf{a}_1 + \mathbf{a}_2$. With hcp-like stacking, the ions in every other plane lie directly above each other (abab...), while with fcc-like stacking, the ions in every third plane are so aligned (abcabc...). When there are 3 or more hexagonal layers, both types of stacking are observed.

The following sequence of phase structures, with lattice

parameters defined in Table 1, is observed as the central areal density σ_0 is increased from where order is first observed: (I) 1-layer hexagonal \rightarrow (III) 2-layer staggered square \rightarrow (IV) 2-layer staggered rhombic \rightarrow (V) 2-layer staggered hexagonal. At a critical density a third layer is formed, resulting in a (III) 3-layer staggered square. The process then repeats with minor variations, such as phase III becoming less common. We have followed here the classifications used in previous theoretical studies of quantum (15) and classical (12) electron bilayer systems. Phase II, which is a stable phase of the bilayer systems where the interlayer distance is fixed, is not listed here because it is unstable for the planar OCP, where this distance is determined by minimization of the system's energy.

We have performed an analytical calculation of the energies of these phase structures for the planar OCP (25). The calculation minimizes the energy (26) of several parallel lattice planes that are infinite and homogeneous in the (x, y) direction but are confined in the \hat{z} -direction by a harmonic external electrostatic confinement potential $\phi_e = 1/2(m/e)\omega_z^2 z^2$. As this potential is identical to the confinement potential of a Penning trap in the $\alpha \rightarrow 0$ planar limit (27), this theory should predict the structures observed in the central region of the lenticular plasmas of the experiments. The predictions of this 2D theory, which has no free parameters, was compared directly with our observations by identifying the σ of the planar OCP with the directly measured central areal density σ_0 of the oblate plasmas. For a quantitative analysis of the observed lattice structure, we performed a least-squares fit of the positions of the ions in the central region to the relevant phases of Table I (lines in Fig. 2). Using the best-fit values of the primitive vector length a and the intralayer angle θ , and the observed number of lattice planes n , the central areal density $\sigma_0 = n/(a^2 \sin \theta)$ was then calculated.

The agreement between the planar OCP theory and experiment, with measurements taken on different plasmas with $N < 10^4$, is good (Figs. 3 and 4). As the central areal density is increased the lattice planes move further apart axially (Fig. 3). Eventually it becomes energetically favorable to form an additional lattice plane. The symbols indicate whether the lattices had an interlattice displacement vector \mathbf{c}_2 characteristic of the hexagonal phases (circles) or the square and rhombic phases (squares). However, although the phase V_{FCC} is predicted to be slightly more energetically favorable than phase V, we rarely observed V_{FCC} ($\sim 5\%$ of the time). These and other minor discrepancies from theory may be due to the finite radial extent of the ion plasma; we note that we observe a similar preference for hcp stacking in molecular dynamics simulations of small ($N=3000$) lenticular ion plasmas.

For the dependence of the angle θ (between the primitive vectors \mathbf{a}_1 and \mathbf{a}_2) on central areal density σ_0 (Fig.

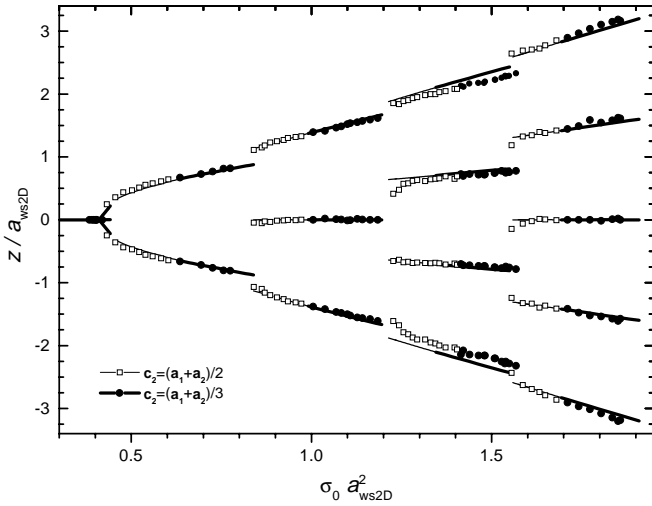


FIG. 3. Interlayer structure (plane axial positions and displacement vectors) of the central region as a function of normalized central areal charge density. The lines are predictions from theory, and the symbols are experimental measurements. Lengths have been normalized by $a_{ws2D} = (3e^2/4\pi\epsilon_0 m\omega_z^2)^{1/3} = 10.7 \text{ } \mu\text{m}$, which is the Wigner-Seitz radius in the planar limit.

4), the general trend is that when a new lattice plane is formed, θ changes discontinuously from $\approx 60^\circ$ to a higher value. As σ_0 of the crystal is further increased, θ smoothly decreases to $\approx 65^\circ$ until there is a second discontinuous transition to a hexagonal structure. This second transition has been predicted to become continuous, with θ assuming all values $60^\circ \leq \theta \leq 90^\circ$, in liquid ($\Gamma < 80$) bilayer systems (28). The lines indicate the minimum energy structures predicted by the 2D theory. At central areal charge densities near phase boundaries, both phases can be observed. In these regions, the phase which materializes after the crystal is formed is initially random, but tends to persist if the ions are not heated. Where there was not a strong preference for one phase over the other, we plot both.

Like most materials, the hexagonal and square phases contract in lateral directions when elongated. However, the rhombic phase shows quite different behavior because the intralayer angle θ strongly depends on the \hat{z} -axis strain: one rhombus diagonal contracts and the second expands when the rhombic phase is elongated in the \hat{z} -axis direction. The dimensional change for the latter diagonal corresponds to a negative value of the Poissons ratio (which is the ratio of the lateral contraction to the longitudinal elongation). The present experimental observations substantially expand the mass density range over which negative Poissons ratios have been established, from $\sim 10 \text{ g/cm}^3$ for cubic metals (29) and $\sim 0.1 \text{ g/cm}^3$ for reentrant foams (30) to $\sim 10^{-15} \text{ g/cm}^3$ for the present ion crystals.

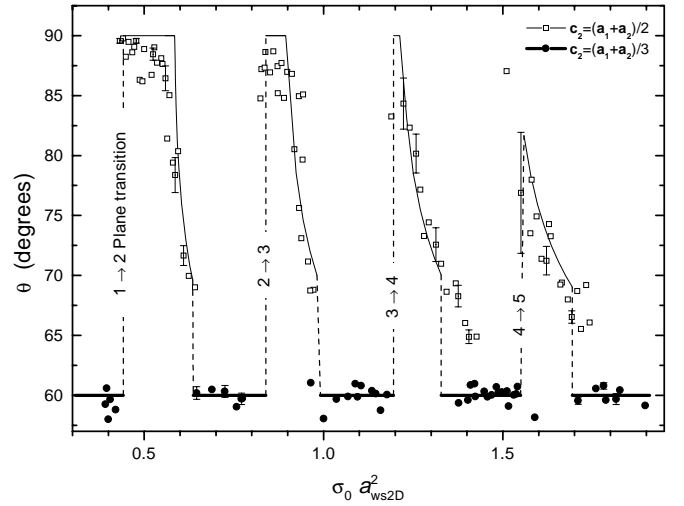


FIG. 4. Intralayer angle θ of the central region as a function of central areal charge density. The lines are predictions from theory and the symbols are experimental measurements from the same data sets which were used in Fig. 3. Representative error bars are included with some of the measurements.

1. H. M. Van Horn, *Science* **252**, 384 (1991).
2. C. C. Grimes, G. Adams, *Phys. Rev. Lett.*, **42**, 795 (1979).
3. D. J. Wineland, R. E. Drullinger, F. L. Walls, *Phys. Rev. Lett.* **40**, 1639 (1978).
4. J. N. Tan, J. J. Bollinger, B. M. Jelenković, D. J. Wineland, *Phys. Rev. Lett.* **72**, 4198 (1995); W. M. Itano *et al.*, *Science* **279**, 686 (1998).
5. I. Waki, S. Kassner, G. Birkel, H. Walther, *Phys. Rev. Lett.* **68**, 2007 (1992); G. Birkel, S. Kassner, H. Walther, *Nature* **357**, 310 (1992).
6. P. K. Ghosh, *Ion Traps* (Clarendon, Oxford, 1995).
7. C. W. Roberson and C. F. Driscoll, Eds, *Non-Neutral Plasma Physics* (AIP, New York, 1988).
8. S. Ichimaru, H. Iyetomi, S. Tanaka, *Phys. Rep.* **149**, 91 (1987).
9. D. H. E. Dubin, *Phys. Rev. E* **42**, 4972 (1990).
10. J. P. Schiffer, *Phys. Rev. Lett.* **70**, 818 (1993).
11. D. H. E. Dubin, *Phys. Rev. Lett.* **71**, 2753 (1993).
12. G. Goldoni and F. M. Peeters, *Phys. Rev. B* **53**, 4591 (1996).
13. J. B. Pieper, J. Goree, R. A. Quinn, *J. Vac. Sci. Technol. A* **14**, 519 (1996); H. Totsuji, T. Kishimoto, C. Totsuji, *Phys. Rev. Lett.* **78**, 3113 (1997).

14. D. H. Van Winkle and C. A. Murray, *Phys. Rev. A* **34**, 562 (1986).
15. S. Narasimhan and T.-L. Ho, *Phys. Rev. B* **52**, 12291, (1995); G. Goldoni and F. M. Peeters, *Europhys. Lett.*, **37**, 293 (1997).
16. M. Schmidt and H. Löwen, *Phys. Rev. E* **55**, 7228 (1997).
17. R. Rafac, J. P. Schiffer, J. S. Hangst, D. H. E. Dubin, D. J. Wales, *Proc. Natl. Acad. Sci. USA* **88**, 483 (1991).
18. F. Diedrich, E. Peik, J. M. Chen, W. Quint, H. Walther, *Phys. Rev. Lett.* **59**, 2931 (1987); D. J. Wineland, J. C. Bergquist, W. M. Itano, J. J. Bollinger, C. H. Manney, *Phys. Rev. Lett.* **59**, 2935 (1987).
19. A. Rahman and J. P. Schiffer, *Phys. Rev. Lett.* **57**, 1133 (1986); D. H. E. Dubin and T. M. O'Neil, *Phys. Rev. Lett.* **60**, 511 (1988).
20. S. L. Gilbert, J. J. Bollinger, D. J. Wineland, *Phys. Rev. Lett.* **60**, 2022 (1988).
21. M. Drewsen, C. Brodersen, L. Hornekaer, J. S. Hangst, J. P. Schiffer, *Phys. Rev. Lett.*, in press.
22. X.-P. Huang, J. J. Bollinger, T. B. Mitchell, W. M. Itano, *Phys. Rev. Lett.* **80**, 73 (1998); X.-P. Huang, J. J. Bollinger, T. B. Mitchell, W. M. Itano, *Phys. Plasmas* **5**, 1656 (1998).
23. L. R. Brewer *et al.*, *Phys. Rev. A* **38**, 859 (1988).
24. T. M. O'Neil, *Phys. Fluids* **24**, 1447 (1981); D. J. Larson *et al.*, *Phys. Rev. Lett.* **57**, 70 (1986).
25. T. B. Mitchell, J. J. Bollinger, D. H. E. Dubin, X.-P. Huang, W. M. Itano, submitted to *Phys. Plasmas*. Preprint is available at www.blrdoc.gov/timefreq/ion/index.htm.
26. Minimization of the energy is carried out numerically by allowing the positions of the planes to vary with respect to one another within the external potential, and by varying the lattice structure within the planes. We make the simplifying assumption, consistent with the experimental observations, that the lattice structure of each plane is identical. The areal density σ_{ocp} of the planar OCP is a control parameter that when varied leads to transitions in both the number and lattice structure of the planes. This theory focuses on the minimum potential energy states, neglecting finite temperature effects that may be important, particularly near the continuous phase transitions where large structural fluctuations may occur.
27. T. M. O'Neil and D. H. E. Dubin, *Phys. Plasmas* **5**, 2163 (1998).
28. V. I. Valtchinov, G. Kalman, K. B. Blagoev, *Phys. Rev. E* **56**, 4351 (1997).
29. R. H. Baughman, J. M. Shacklette, A. A. Zakhidov, S. Stafstrom, *Nature* **392**, 362 (1998).
30. R. S. Lakes, *Science* **235**, 1038 (1987).
31. This manuscript is a work of the U.S. government; it is not subject to U.S. copyright. This research was supported by the Office of Naval Research and the National Science Foundation (D. H. E. D.). We thank B. King, R. J. Rafac, J. P. Schiffer and D. J. Wineland for useful comments, and B. M. Jelenković and J. N. Tan for technical assistance.

TABLE I. Primitive and interlayer displacement vectors in (x, y) plane for the observed phases. The primitive vector \mathbf{a}_1 defines the $\hat{\mathbf{x}}$ direction, and $|\mathbf{a}_1| = |\mathbf{a}_2| \equiv \mathbf{a}$. Dashes, not applicable.

Phase	Symmetry	Stacking	\mathbf{a}_1	\mathbf{a}_2	\mathbf{c}_2	\mathbf{c}_3
I	hexagonal	single plane	$(a, 0)$	$(a \cos 60^\circ, a \sin 60^\circ)$	—	—
III	square	staggered	$(a, 0)$	$(0, a)$	$(\mathbf{a}_1 + \mathbf{a}_2)/2$	$(0, 0)$
IV	rhombic	staggered	$(a, 0)$	$(a \cos \theta, a \sin \theta)$	$(\mathbf{a}_1 + \mathbf{a}_2)/2$	$(0, 0)$
V	hexagonal	hcp-like	$(a, 0)$	$(a \cos 60^\circ, a \sin 60^\circ)$	$(\mathbf{a}_1 + \mathbf{a}_2)/3$	$(0, 0)$
V _{FCC}	hexagonal	fcc-like	$(a, 0)$	$(a \cos 60^\circ, a \sin 60^\circ)$	$(\mathbf{a}_1 + \mathbf{a}_2)/3$	$2(\mathbf{a}_1 + \mathbf{a}_2)/3$